

Complex charge density waves in simple electronic systems of two-dimensional $\text{III}_2\text{-VI}_3$ materials

Received: 23 April 2024

Accepted: 31 October 2024

Published online: 18 November 2024

Yu-Ting Huang¹, Zhen-Ze Li^{1,2}, Nian-Ke Chen¹✉, Yeliang Wang³,
Hong-Bo Sun^{1,2}, Shengbai Zhang⁴ & Xian-Bin Li¹✉

Charge density wave (CDW) is the phenomenon of a material that undergoes a spontaneous lattice distortion and modulation of the electron density. Typically, the formation of CDW is attributed to Fermi surface nesting or electron-phonon coupling, where the CDW vector (\mathbf{Q}_{CDW}) corresponds to localized extreme points of electronic susceptibility or imaginary phonon frequencies. Here, we propose a new family of multiple CDW orders, including chiral Star-of-David configuration in nine 2D $\text{III}_2\text{-VI}_3$ van der Waals materials, backed by first-principles calculations. The distinct feature of this system is the presence of large and flat imaginary frequencies in the optical phonon branch across the Brillouin zone, which facilitates the formation of the diverse CDW phases. The electronic structures of 2D $\text{III}_2\text{-VI}_3$ materials are relatively simple, with only $\text{III-}s,p$ and $\text{VI-}p$ orbitals contributing to the formation of the CDW order. Despite that, the CDW transitions involve both metal-to-insulator and insulator-to-insulator transitions, accompanied by a significant increase in the bandgap caused by an enhanced electronic localization. Our study not only reveals a new dimension in the family of 2D CDWs, but is also expected to offer deeper insights into the origins of the CDWs.

The concept of charge density wave (CDW) refers to the phenomena of periodic modulation of solid lattice and charge density^{1–3}. The formation of CDW is often accompanied by other interesting physical properties such as ferroelectric^{4,5}, superconductivity^{6–10}, magnetism^{11–13}, and Mott insulation^{14–16}, thus attracting extensive attention in the field of condensed matter physics. Typically, CDWs can be divided into three categories according to their origin¹⁷. Type I CDWs often occur in quasi-one-dimensional systems and can be regarded as an analog of the Peierls instability. Lattice vibration will be effectively screened by the zero electronic excitation at the Fermi surface nesting (FSN) vector, and a dimerized, metal-to-insulator transition occurs, lowering the energy of the ground state^{18–23}. However, the simple physical picture of

FSN is difficult to generalize to two-dimensional (2D) or three-dimensional physical systems. In this case, the \mathbf{k} -dependent electron-phonon coupling (EPC) plays a crucial role, which leads to the emergence of the concept of type II CDWs. The typical feature of such a CDW system is the coincidence of \mathbf{Q}_{CDW} with the peak of the phonon linewidth, which corresponds to the localized imaginary frequencies of phonon branches that trigger the CDW structural transition. Most 2D CDW materials such as 2H-NbSe_2 , and 1T-VSe_2 ^{24–26}, can be classified as Type II CDWs, and the instability of electron and lattice structures in these materials is closely correlated. There still exist unconventional Type III CDW materials such as cuprates. Although the possible presence of FSN or EPC in these materials, there is no clear evidence

¹State Key Laboratory of Integrated Optoelectronics, College of Electronic Science and Engineering, Jilin University, Changchun, China. ²State Key Laboratory of Precision Measurement Technology and Instruments, Department of Precision Instrument, Tsinghua University, Beijing, China. ³School of Integrated Circuits and Electronics, MIIT Key Laboratory for Low-Dimensional Quantum Structure and Devices, Beijing Institute of Technology, Beijing, China.

⁴Department of Physics, Applied Physics, and Astronomy, Rensselaer Polytechnic Institute, Troy, NY, USA. ✉e-mail: chennianke@jlu.edu.cn; lixianbin@jlu.edu.cn

indicating that these factors explicitly determine the formation of specific CDW configurations, whereas the strong electron correlation effect may play a role²⁷. Since the origin of CDW remains controversial as its properties are highly material-dependent, exploring unique CDW is of significant importance for understanding their property and origin.

In this work, we unveil unexpected multiple CDW orders in 2D $\text{III}_2\text{-VI}_3$ (III = Al, Ga, In; VI = S, Se, Te) materials, represented by the chiral Star-of-David (c-SoD) configuration of 2D In_2Se_3 , backed by first-principles calculations. Compared with traditional SoD CDW materials such as 1T-TaS_2 , which exhibits strong electronic correlation^{28–31}, the electronic structures of 2D $\text{III}_2\text{-VI}_3$ materials are quite simple, with only *s*- and *p*-orbitals observable near the Fermi level. We found it is the flat optical phonon branch with significant imaginary frequencies [induced by the Mexican-hat potential energy surface (PES)] distributed over a considerable range of the Brillouin zone that facilitates the formation of a large number of stable/metastable CDW phases. Calculations show that the energies of these CDW phases are close to each other, and in contrast to the widely-studied type II CDWs, their Q_{CDW} do not always correspond to the local minimum of the phonon branch, implying that the EPC is not the sole factor determining the specific CDW configuration. Through electronic band structure analyses, we found that the CDW transitions in 2D $\text{III}_2\text{-VI}_3$ materials are

accompanied by an enhancement of electron localization and a more significant bandgap opening compared to other 2D CDWs. This suggests that the observed CDW in 2D $\text{III}_2\text{-VI}_3$ materials may originate from the “locking” of specific chemical bonding provided by the broad freedom of the Mexican-hat PES. Our discovery of complex CDWs induced by flat phonon branch with significant imaginary frequencies in simple electronic systems is expected to provide deeper insights into the origins of CDWs.

Results

c-SoD CDW in 2D $\beta\text{-In}_2\text{Se}_3$

2D In_2Se_3 has attracted widespread attention in recent years due to its robust ferroelectricity at the ultrathin thickness limit^{32–34}. One of the most important features of 2D In_2Se_3 is the diversity of phases, such as α , β , γ phases, etc³⁴. Figure 1a shows the schematic diagram of the atomic structure of undistorted high-symmetry monolayer $\beta\text{-In}_2\text{Se}_3$ ($\beta\text{-In}_2\text{Se}_3$), where the middle layer Se [*Se(m)*] atoms are located at the center of each unit cell. It has a five-atomic-sublayer structure arranged in the order of Se-In-Se-In-Se and exhibits an inversion symmetry centered on Se(*m*) atoms. Previous calculations have demonstrated the energetic instability of 2D $\beta\text{-In}_2\text{Se}_3$, consequently, the Se(*m*) atoms will deviate from the central position along a unified direction, leading to an in-plane ferroelectric polarization^{34,35}. Surprisingly, we found that

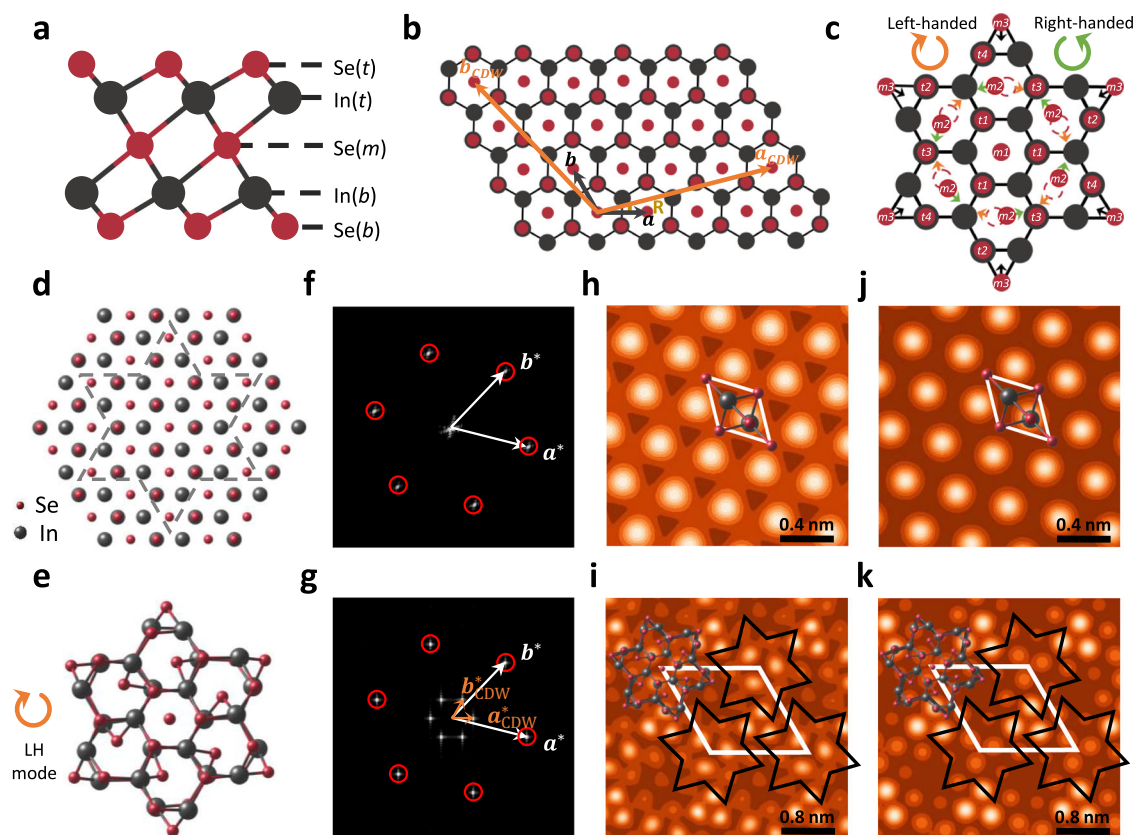


Fig. 1 | Atomic structures and simulated scanning tunneling microscope (STM) patterns of the pristine high-symmetry phase and chiral Star-of-David (c-SoD) charge density wave (CDW) phase of monolayer $\beta\text{-In}_2\text{Se}_3$. **a** Schematic side view of the atomic structure of the pristine high-symmetry monolayer $\beta\text{-In}_2\text{Se}_3$ ($\beta\text{-In}_2\text{Se}_3$). **b** Top view of the lattice vectors of monolayer $\beta\text{-In}_2\text{Se}_3$ (black arrows) and the c-SoD reconstructed phase (orange arrows), the rotation angle between the two sets of lattices is $R = 13.9^\circ$. **c** Schematic diagram of the displacement of the middle layer Se [*Se(m)*] atoms during the $\beta\text{-In}_2\text{Se}_3$ to c-SoD CDW transition, where Se(*m*) atoms are marked as Se(*m1*), Se(*m2*), Se(*m3*) and Se(*t*) atoms are marked as Se(*t1*), Se(*t2*), Se(*t3*), Se(*t4*) according to their locations. The CDW transition can be named the left-handed (LH) mode and right-handed (RH) mode according to the clockwise or

counterclockwise motions of Se(*m2*) atoms. Top view of the actual atomic structures of **(d)** $\beta\text{-In}_2\text{Se}_3$ and **(e)** LH-c-SoD phases of monolayer In_2Se_3 . The c-SoD configuration is formed by the atoms enclosed by the gray dotted line in Fig. 1d being twisted together according to the LH mode. **f, g** Diagram of the reciprocal lattice vectors extracted from the fast Fourier-transform mapping of the atomic structures of the $\beta\text{-In}_2\text{Se}_3$ and c-SoD phases of monolayer In_2Se_3 . White and orange arrows represent the reciprocal lattice vectors of $\beta\text{-In}_2\text{Se}_3$ (a^* and b^*) and c-SoD (a_{CDW}^* and b_{CDW}^*) phase of 2D In_2Se_3 , respectively. Density functional theory simulated STM images of the **(h, i)** empty and **(j, k)** filled states of $\beta\text{-In}_2\text{Se}_3$ and LH-c-SoD phases, the simulated bias voltages are +2 V and −2 V, respectively.

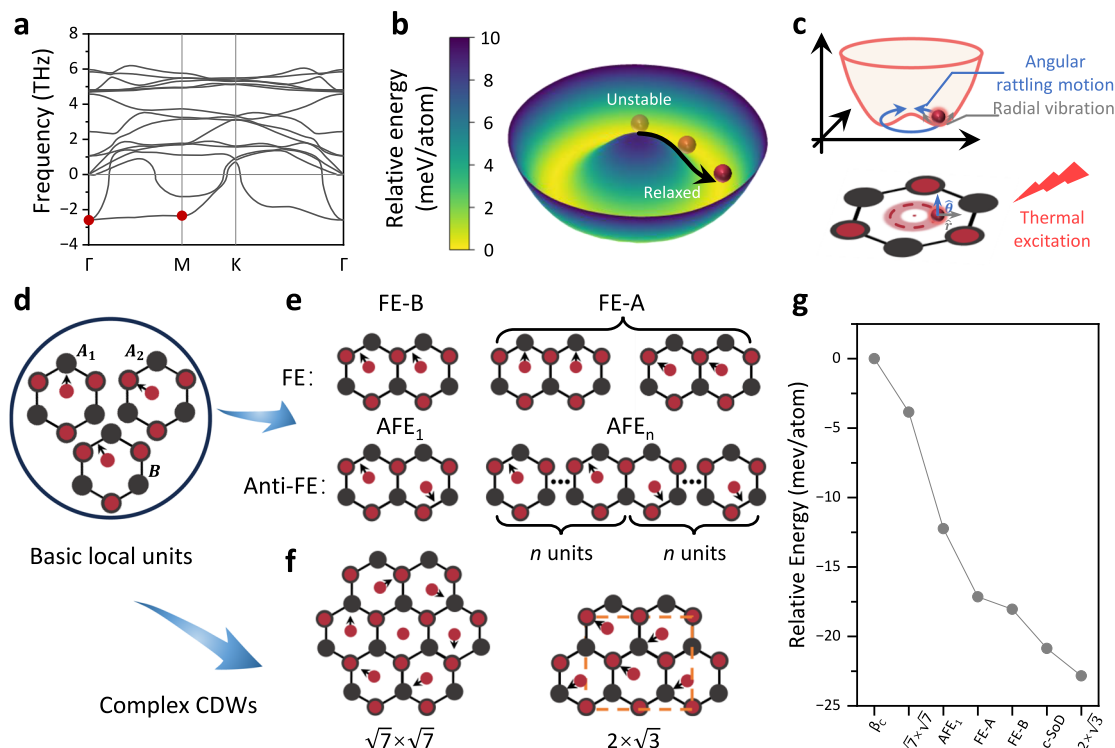


Fig. 2 | Diversity of CDWs in 2D β - In_2Se_3 . **a** Phonon band structure of monolayer β_c - In_2Se_3 with significant imaginary frequencies. Two red dots highlight specific phonon modes which will be discussed later. **b** In-plane Mexican-hat potential energy surface (PES) of $\text{Se}(m)$ atom of 2D β_c - In_2Se_3 . **c** The schematic diagram of the angular rattling motion and radial vibration of $\text{Se}(m)$ atom with a Mexican-hat

PES under thermal excitation. **d** Three basic local units of the CDW phase. **e** The ferroelectric (FE) and antiferroelectric (AFE) phases with parallel and antiparallel arrangement of basic local units. **f** The $\sqrt{7} \times \sqrt{7}$ and $2 \times \sqrt{3}$ CDW orders that formed by the specific arrangement of basic local units. **g** The relaxed energies of various CDW phases, using the energy of β_c phase as a reference.

by taking the lattice vectors as $\mathbf{a}_{\text{CDW}} = 4\mathbf{a} + \mathbf{b}$ and $\mathbf{b}_{\text{CDW}} = -\mathbf{a} + 3\mathbf{b}$, where \mathbf{a} and \mathbf{b} marked by the black arrows in Fig. 1b are the lattice vectors of β_c phase, the spatial translational invariance of $\text{Se}(m)$ displacements can be broken, and a new CDW phase can be formed. Figure 1c illustrates the distortions of $\text{Se}(m)$ atoms during the formation of CDW, in which one of the $\text{Se}(m)$ atoms serves as the center of the CDW, denoted as $\text{Se}(m1)$, and its six nearest-neighboring $\text{Se}(m)$ atoms, labeled as $\text{Se}(m2)$ will rotate clockwise (left-handed, LH) or counterclockwise (right-handed, RH), leading to a ferroelectric dipole vortex pattern. At the same time, six $\text{Se}(m3)$ atoms shrink toward the $\text{Se}(m1)$ atom, and finally a $\sqrt{13} \times \sqrt{13}$ c-SoD configuration is formed. Here, the chirality is used to define the rotation direction of $\text{Se}(m2)$ atoms. Figure 1d, e shows the top view of the atomic structure of β_c and c-SoD phases. In an actual situation, the LH-c-SoD configuration in Fig. 1e can be formed by the displacement of the atoms enclosed by the gray dashed line in Fig. 1d.

The white and orange arrows in Fig. 1f, g mark the reciprocal lattice vectors of the β_c and c-SoD phases of 2D In_2Se_3 , respectively, which are extracted by the fast Fourier transform of the corresponding atomic structures. Their relation follows the formula: $\mathbf{a}_{\text{CDW}}^* = \frac{3}{13}\mathbf{a}^* + \frac{1}{13}\mathbf{b}^*$, $\mathbf{b}_{\text{CDW}}^* = -\frac{1}{13}\mathbf{a}^* + \frac{4}{13}\mathbf{b}^*$, matching the lattice reconstruction in real space. Density functional theory (DFT) simulated scanning tunneling microscope (STM) images of the empty and filled states of β_c and c-SoD phases are shown in Fig. 1h–k, the simulated bias voltages are +2 V (Fig. 1h, i) and −2 V (Fig. 1j, k), respectively. It can be seen that the hexagonal lattice and three-fold rotational symmetry of 2D β_c - In_2Se_3 are still preserved, but the mirror symmetry is broken. Additionally, the lattice constant increases from 4.0 to 14.6 Å after the c-SoD CDW transition. Combining the vertical positions and the partial density of states (PDOS) shown in Supplementary Fig. 2 of Supplementary Note 2, bright spots of the β_c phase in Fig. 1h, j are contributed

by the top layer $\text{Se}(\text{Se}(t))$ atoms. However, the $\text{Se}(t)$ atoms of the c-SoD phase will fluctuate in the vertical direction due to CDW distortion, and they can be divided into four categories, named $\text{Se}(t1-4)$, as shown in Fig. 1c. The height sequence of these atoms from top to bottom is $\text{Se}(t2) > \text{Se}(t1) > \text{Se}(t4) > \text{Se}(t3)$. Combined with the PDOS in Supplementary Fig. 3 of Supplementary Note 2, the brightness order of the spots in the STM patterns in Fig. 1i, k from bright to dark is $\text{Se}(t2) > \text{Se}(t1) > \text{Se}(t4) \approx \text{Se}(t3)$. The dynamical stability of the c-SoD phase at 200 K is confirmed through molecular dynamics (MD) simulations in Supplementary Fig. 4 of Supplementary Note 3. In comparison with the SoD-reconstructed CsV_3Sb_5 and 1T-TaS₂, whose CDW stable temperatures in experiments are about 94 K and 180 K^{36,37}, respectively, the 2D β - In_2Se_3 predicted in this study exhibits strong thermal stability.

Then, the question arises: what is the physical origin of this c-SoD? Firstly, considering the high-symmetry β_c - In_2Se_3 as a semiconductor has a nonzero bandgap, the theory of FSN is not applicable³⁸. Furthermore, if we assume that 2D β_c - In_2Se_3 belongs to the type II CDW, the phonon spectrum is expected to exhibit localized imaginary frequencies at \mathbf{Q}_{CDW} due to strong EPC, similar to what is observed in 1T-VSe₂ and 2H-NbSe₂^{39,40}. However, the phonon spectrum analysis in Fig. 2a reveals that 2D β_c - In_2Se_3 exhibits surprisingly flat and significant imaginary frequencies across a wide range of reciprocal space, with no localized phonon imaginary frequency observed at the \mathbf{Q}_{CDW} of the c-SoD phase.

Diversity of CDWs in 2D β - In_2Se_3

We indicate that although EPC is not the exclusive factor leading to the emergence of c-SoD, the significant flat phonon imaginary frequencies lay a crucial foundation for the multi-CDW orders in 2D β - In_2Se_3 . Firstly, DFT calculations indicate that the phonon imaginary frequencies are attributed to the Mexican-hat PES of $\text{Se}(m)$ atoms³⁵. As

shown in Fig. 2b, the local maximum of the PES is located at the centrosymmetric position of 2D β - In_2Se_3 . Hence, the $\text{Se}(m)$ atom is expected to deviate from the center site and fall into the basin. Considering the symmetry of the crystal, there should be 12 minima on the basin, and the stable positions of $\text{Se}(m)$ atoms can be categorized into three types as shown in Fig. 2d. According to the distortion direction of $\text{Se}(m)$ atoms, these configurations can be named as \mathbf{A}_1 (distort towards In atoms), \mathbf{A}_2 (distort towards Se atoms), and \mathbf{B} (distort towards In-Se bonds). Therefore, if each $\text{Se}(m)$ atom within a unit cell slides into the same distorted configuration, ferroelectric (FE) phases with all dipoles consistently aligned can be obtained, as shown by FE-A and FE-B in Fig. 2e. The existence of these FE phases has also been experimentally confirmed⁴¹. From the perspective of the EPC effect, the formation of FE phases can be attributed to the imaginary phonon modes at the Γ point marked by the red dot in Fig. 2a. The eigenmotions of these two degenerate modes involve the in-phase vibrations of $\text{Se}(m)$ atoms in the in-plane direction, as detailed in the Supplementary Fig. 5 of Supplementary Note 4.

However, since the basin of the PES is nearly flat, the $\text{Se}(m)$ atom in each unit cell may distort towards different configurations at finite temperatures. This suggests that c-SoD may not be the only CDW configuration in 2D β - In_2Se_3 , and the flat imaginary phonon modes may induce the generation of multiple CDW orders. Hence, the translation invariance of the original lattice vectors of 2D β - In_2Se_3 is broken. Figure 2c illustrates the schematic diagram of $\text{Se}(m)$ atoms independently undergoing angular oscillation along $\hat{\theta}$ and radial vibration along \hat{r} within the basin of the PES under the thermal excitation. Therefore, the spatially uneven fluctuations of each $\text{Se}(m)$ atom can lead to the formation of distinct configurations with local energy minima, subsequently inducing complex CDW orders, such as the aforementioned c-SoD phase. Along these lines, a series of 2D β - In_2Se_3 phases can be constructed. The three off-center primitive cells (\mathbf{A}_1 , \mathbf{A}_2 , and \mathbf{B}) that triggered by the significant imaginary frequencies together with the centrosymmetric cell [i.e., $\text{Se}(m)$ at the center of the Mexican-hat PES, named \mathbf{C}], can be served as the basic units of the CDW orders. When basic units with opposite distortion directions coexist in equal amounts and orderly manner (such as an equal combination of \mathbf{B} and $-\mathbf{B}$, where the “minus” denotes the opposite direction of atomic distortion), 2D β - In_2Se_3 can exist in the form of an antiferroelectric (AFE) phase, which is also consistent with recent experimental observations⁴². Figure 2e shows the AFE phase with opposite polarizations of adjacent units, and from the perspective of EPC effect, it corresponds to the opposite vibrations of adjacent $\text{Se}(m)$ atoms. For the lowest (imaginary-frequency) phonon branch along the Γ -M path in Fig. 2a, there are also eigen vibrations of $\text{Se}(m)$ atoms along the lattice vector \mathbf{a} , but with a phase difference. For the mode marked by the red dot at point M, the neighboring $\text{Se}(m)$ atoms vibrate out of phase, which may correspond to the formation of the AFE phase, the detailed eigen motions are presented in Supplementary Fig. 5 of Supplementary Note 4. In addition to the AFE phase, c-SoD phase with opposite chirality, namely, the antichiral SoD (ac-SoD) phase with similar energies, can also be formed in monolayer β - In_2Se_3 , the detailed atomic structures are shown in Supplementary Fig. 6 of Supplementary Note 5.

Additionally, through the combination of basic local units with different distortion directions, more complex CDW orders can be formed. For example, we also predict a new $\sqrt{7} \times \sqrt{7}$ CDW phase which is formed by the clockwise/counterclockwise motion of the six nearest neighboring $\text{Se}(m2)$ atoms centered around one $\text{Se}(m1)$ atom, similar to the $\sqrt{13} \times \sqrt{13}$ c-SoD phase. The schematic diagram of the atomic structure is shown in Fig. 2f, it can be seen as a combination of three \mathbf{A}_1 units, three \mathbf{A}_2 units, and one \mathbf{C} unit. Besides, when the basic units are combined in the form of two \mathbf{A}_1 units and two \mathbf{A}_2 units, the in-plane ferroelectric $2 \times \sqrt{3}$ configuration CDW order can be formed. The relaxed atomic structures

of the above CDW orders are presented in Supplementary Fig. 7 of Supplementary Note 6.

For CDW phases with relatively simple configurations, such as the FE phase and AFE phase, we can easily identify soft phonon modes that correspond to their \mathbf{Q}_{CDW} in the phonon spectrum (red dots in Fig. 2a). However, for complex CDW orders such as the $\sqrt{13} \times \sqrt{13}$ (c-SoD), $\sqrt{7} \times \sqrt{7}$ and $2 \times \sqrt{3}$, pinpointing the localized unstable phonon modes that correspond to their order vectors becomes challenging, which implies that the complex CDW configuration may be a superposition of multiple soft phonon modes. Finally, we compared the energies of different phases in Fig. 2g, all of which exhibit significantly lower energies than the undistorted β -phase. It is worth noting that the AFE phases are stripe-like, and their total energies also depend on the width of stripe⁴³. In Fig. 2g, we show the energy of the AFE₁ phase as a representative. A more comprehensive energy comparison of the AFE phases is provided in Supplementary Fig. 8 of Supplementary Note 6. In addition, the energies of the $2 \times \sqrt{3}$ phase and the c-SoD phase are very close to each other. Considering that the $2 \times \sqrt{3}$ CDW phase has been experimentally confirmed to be stable at 170 K⁴⁴. Therefore, we predict that the c-SoD phase may also be experimentally stable in a similar temperature range, which is also consistent with the stability deduced from the MD in Supplementary Fig. 4. The current experimental observations of the in-plane polarized $2 \times \sqrt{3}$ phase are achieved by cooling the FE β phase, which also has an in-plane ferroelectricity as the seed for the transition. However, to obtain the centrosymmetric c-SoD phase (with zero net electric dipole moment) in experiments, we suggest one should eliminate the ferroelectric seed in the FE β phase before cooling the temperature, possibly with effective methods like optically electronic excitation or electron doping⁴⁵.

Origin of CDW in 2D β - In_2Se_3

In addition to the periodic modulation of the charge density, the significant opening of the bandgap is another important feature of CDWs in 2D β - In_2Se_3 . Here, taking the c-SoD phase of 2D In_2Se_3 as an example, we calculated its PBE band structure before and after the CDW transition, respectively. For a better comparison, both calculations were conducted using a $\sqrt{13} \times \sqrt{13}$ reconstructed cell. The results in Fig. 3a, b show that after the c-SoD CDW distortion, the PBE energy bandgap increases from 0.49 eV to 1.38 eV. Unlike previously reported SoD CDW materials, such as 1T-NbSe₂ whose bandgap opening is induced by the splitting of *d*-orbitals-related Hubbard band¹⁴, the electronic structure of 2D β - In_2Se_3 is relatively simple. The PDOS in Fig. 3a, b show that the orbitals near the Fermi level consist only of In-*s*, *p*, and Se-*p* states. To further demonstrate that the *d*-orbitals are not necessary for the formation of CDW, we performed structural relaxation and electronic band structure calculations of the c-SoD phase but used the pseudopotential that excludes the 4*d*-orbitals of In atoms. As shown in Supplementary Fig. 9 of Supplementary Note 7, the band structure is consistent with that (considering the 4*d*-orbitals of In atoms) in Fig. 3b.

Furthermore, we conducted integrated crystal orbital bond index (ICOBI) analysis and charge density difference (CDD) calculations, attempting to provide insights into the bandgap increase from the perspectives of changes in electron localization and local covalency of In-Se bonds. ICOBI is an intuitive parameter to quantify the covalency of chemical bonds, with the value closer to 1 indicating stronger covalency⁴⁶. Figure 3c shows the ICOBI of In-Se bonds in the c-SoD phase, with gray scatter points indicating the In(*t* or *b*)-Se(*t* or *b*) bonds and red scatter points representing the In(*t* or *b*)-Se(*m*) bonds. The In(*t* or *b*)-Se(*t* or *b*) and In(*t* or *b*)-Se(*m*) bonds of pristine 2D β - In_2Se_3 used for reference are marked with gray and red pentagrams, respectively. After the c-SoD CDW transition, the bond length of In(*t* or *b*)-Se(*t* or *b*) slightly changes from 2.68 Å to a range of 2.62–2.79 Å, and the ICOBI changes from 0.69 to a range of 0.56–0.83. In contrast, the In(*t* or *b*)-

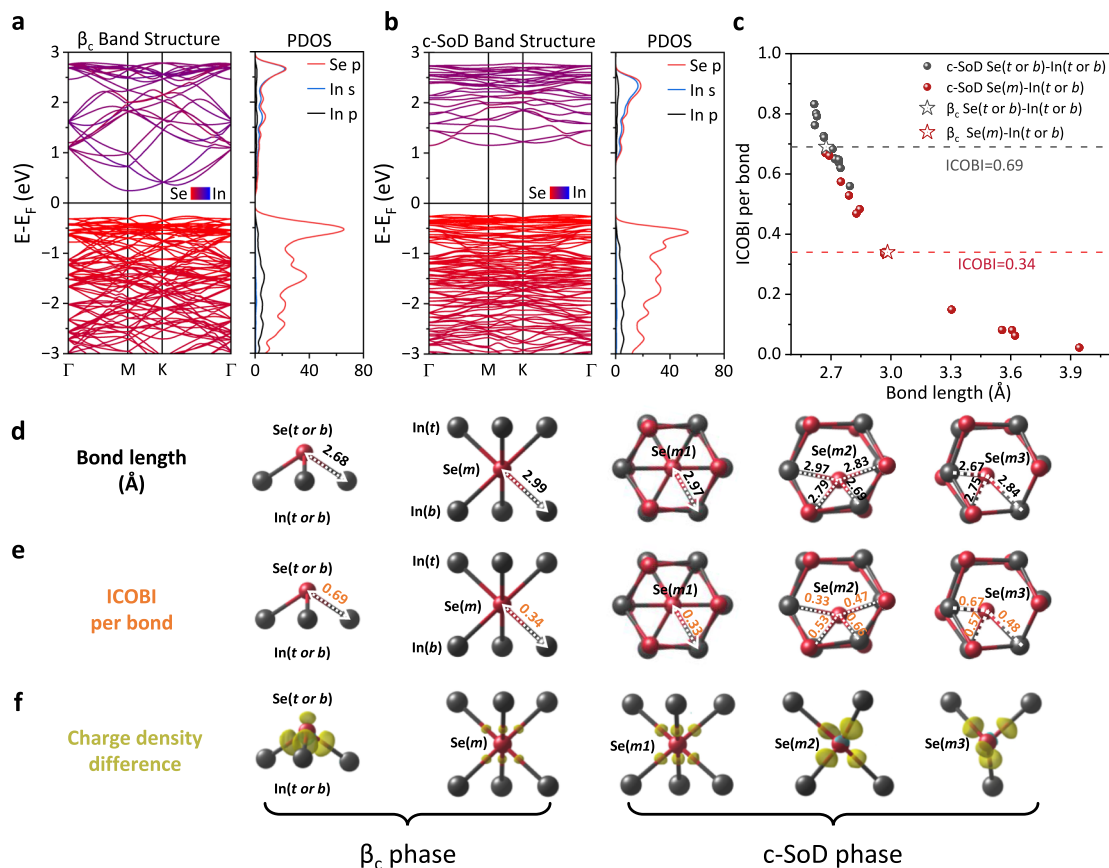


Fig. 3 | Changes in electronic structure and chemical bonds of 2D β - In_2Se_3 before and after the c-SoD CDW transition. PBE band structures and partial density of states (PDOS) of the (a) β_c phase (using the $\sqrt{13} \times \sqrt{13}$ supercell) and the (b) $\sqrt{13} \times \sqrt{13}$ c-SoD CDW phase of 2D In_2Se_3 . c Integrated crystal orbital bond index (ICObI) (per bond) varies with the length of In-Se bond in the c-SoD phase, the red and gray dashed lines mark the ICObI of the In(t or b)-Se(m) and In(t or b)-Se(t or b) bonds in the β_c phase, respectively. d–f Bond length, ICObI, and the local

charge density difference (CDD) of the β_c and c-SoD CDW phases. The CDD is defined as $\Delta\rho = \rho_{scf} - \rho_{atom}$, where ρ_{scf} represents the charge density of In_2Se_3 compound and ρ_{atom} is the superposition of charge density of isolated In and Se atoms. The displaying In-Se bond length cutoff is 3 Å. The isosurface value of CDD is 0.0065 e/a_0^3 , a_0 is the Bohr radius. Yellow isosurface represents charge accumulation.

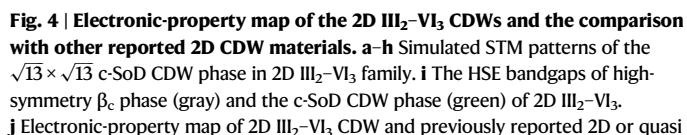
Se(m) bond has undergone more significant changes, with length changing from 2.99 Å to the range of 2.67–3.94 Å, and the ICObI changing from 0.34 to the range of 0.02–0.67. This illustrates the dominant role of the Mexican-hat PES and the flat soft phonon modes. Figure 3d–f mark the length, ICObI, and CDD of In-Se bonds in the β_c and c-SoD phases with a 3.00 Å displaying bond length cutoff. These results indicate that the CDW transition is accompanied by the break of a significant number of In(t or b)-Se(m2 or m3) bonds. For those In(t or b)-Se(m) bonds whose lengths are shortened, the concentration of charge on the bonds increases, leading to an enhancement in electron localization. Simultaneously, the ICObI of these In(t or b)-Se(m) bonds also increases, indicating strengthened covalency. The complete CDD images of β_c and c-SoD phase are shown in Supplementary Fig. 10 of Supplementary Note 8.

Based on the above analysis, it can be concluded that the formation of CDW is inseparable from the distortion of Se(m) atoms and the enhancement of electron localization (or local covalency). On one hand, the distortions of Se(m) atoms are empowered by their intrinsic Mexican-hat PES and flat soft phonon modes, which introduce a new degree for regulating the configuration of CDW. On the other hand, the electron localization and local covalency of chemical bonds in the specific configuration is significantly enhanced, resulting in bandgap opening and a decrease in energy, thereby locking the CDW order and maintaining its stability. Furthermore, we calculated the PBE band structures of the other six CDW configurations

mentioned in Fig. 2e, f. The results in Supplementary Fig. 11 of Supplementary Note 9 exhibit a significant increase in bandgap after the CDW transitions.

Universality of CDW in 2D β - $\text{III}_2\text{-VI}_3$

Considering that the Mexican-hat PES was confirmed to be a general phenomenon in 2D β - $\text{III}_2\text{-VI}_3$ materials (III = Al, Ga, In; and VI = S, Se, Te)³⁵, then CDW in 2D In_2Se_3 should also be prevalent in the other eight materials. Through structural relaxation, we indeed identified the other eight c-SoD CDW configurations. The local atomic structures and the DFT-simulated STM patterns are shown in Fig. 4a–h, the detailed atomic structures are presented in Supplementary Fig. 12 of Supplementary Note 10. The STM patterns of these eight materials all exhibit the same $\sqrt{13} \times \sqrt{13}$ lattice periodicity and three-fold symmetry as those of the c-SoD phase of 2D In_2Se_3 . Previous studies have suggested that CDW transitions are often accompanied by a metal-to-insulator transition. However, the situation is more diverse in 2D $\text{III}_2\text{-VI}_3$ compounds. Here, using the higher-level hybrid functional (HSE06), we calculated the band structures of nine 2D $\text{III}_2\text{-VI}_3$ compounds. The bar charts in Fig. 4i indicate that the bandgaps of their β_c phase range from 0 to 2.4 eV, while the bandgaps of the nine c-SoD CDW phases are in the range of 0.9–3.5 eV, suggesting that there are both metal-to-insulator and insulator-to-insulator CDW transitions in 2D $\text{III}_2\text{-VI}_3$. The PBE and HSE06 band structures of the β_c and c-SoD phases of 2D $\text{III}_2\text{-VI}_3$ materials are also shown in Supplementary Figs. 13–16 of Supplementary Note 11.



–2D CDW materials, the horizontal axis indicates the bandgap of the pristine high-symmetry phase, and the vertical axis indicates the bandgap of the CDW phase. The purple circle marked with coordinates (0, 0) encompasses materials in which the bandgap remains zero both before and after the CDW transition. All the bandgaps of the previously reported materials are obtained from the published literature^{14,47–59}.

Discussion

Through first-principles calculations, STM simulations, and MD simulations, the $\sqrt{13} \times \sqrt{13}$ c-SoD reconfigured CDW phase is first discovered in 2D β - In_2Se_3 and the entire family of 2D β - III_2 - VI_3 . Different from traditional SoD CDW materials such as NbSe_2 or TaS_2 , which have electrons in d -orbitals that exhibit strong correlation characteristics, the electronic structures of 2D III_2 - VI_3 materials are rather simple with only s - and p -orbitals observed near the Fermi-level. However, due to the flat and extensive imaginary phonon frequencies and the Mexican-hat PES of the $\text{Se}(m)$ atoms, the CDW orders of 2D β - In_2Se_3 are complex and diverse, which bring physical phenomena such as atomic-scale ferroelectric vortex in the c-SoD CDW. Through the analysis of the electronic structure and chemical bonds, we found that specific CDW configurations can be stabilized by the localized enhancement of covalency induced by the distorted $\text{Se}(m)$ atoms. Simultaneously, the CDW transition is accompanied by an increased degree of electron localization, which results in significantly wider bandgaps in 2D III_2 - VI_3 materials compared to traditional 2D CDW materials. Our work provides a new branch of CDW materials and expands its electronic-property map, which may bring new insights and platforms for future

study on the origin of CDWs, and even the design of next-gen electronic devices.

Methods

DFT calculations

In this study, the Vienna ab initio simulation package (VASP) was used for DFT calculations⁶⁰. The projector augmented wave (PAW) pseudopotential and the Perdew–Burke–Ernzerhof (PBE) exchange–correlation functional were employed^{61,62}. The *4d*, *5s*, and *5p* orbitals of In atoms, and the *4s* and *4p* orbitals of Se atoms are considered. The Monkhorst–Pack k-points grid for geometry optimization of the high-symmetry β_c and the $\sqrt{13} \times \sqrt{13}$ c-SoD phases of 2D $\text{III}_2\text{-VI}_3$ materials are $13 \times 13 \times 1$ and $5 \times 5 \times 1$, respectively. The k-points grids for static energy calculation of the two phases are $17 \times 17 \times 1$ and $6 \times 6 \times 1$, respectively. It is noteworthy that the crystal cell of the high-symmetry 2D $\beta_c\text{-In}_2\text{Se}_3$ was also enlarged to a $\sqrt{13} \times \sqrt{13}$ supercell for a better comparison when performing PBE band structure calculations. The energy cutoff for geometry optimization and static calculations was 311 eV. To obtain the more accurate bandgaps of 2D $\beta\text{-III}_2\text{-VI}_3$ materials before and after the CDW distortions, the Heyd–Scuseria–Ernzerhof hybrid functional (HSE06)⁶³ with a mixing parameter of 25% was used. A vacuum region with thickness of 20 Å is constructed in the vertical direction of all cells to reduce the influence of periodic boundaries, and the *c*-axis of the cell was fixed during the geometry optimization calculations. A $2 \times 2 \times 1$ supercell of the $\sqrt{13} \times \sqrt{13}$ c-SoD phase containing 260 atoms was constructed for MD simulations and the NVT ensemble was employed⁶⁴. The timestep was set to 1 fs and the energy cutoff was 250 eV. The ICOBI of In–Se bond is calculated using the LOBSTER package⁶⁵. The simulated STM patterns were obtained using the VASP package and the VASPKIT⁶⁶ processing program. The phonon band structure is calculated using the Phonopy code⁶⁷, and the convergence tests are given in Supplementary Fig. 1. Further details about the calculations are provided in Supplementary Note 1.

Data availability

The data supporting the findings of this work are available within the article and Supplementary Information. All data are available from the corresponding authors.

Code availability

The DFT calculations have been carried out using the VASP software⁶⁰. The simulated STM patterns were obtained using the VASPKIT code⁶⁶. The ICOBI of In–Se bond is calculated using the LOBSTER package⁶⁵.

References

- Moncton, D. E., Axe, J. D. & DiSalvo, F. J. Study of superlattice formation in 2H-NbSe_2 and 2H-TaSe_2 by neutron scattering. *Phys. Rev. Lett.* **34**, 734–737 (1975).
- Grüner, G. The dynamics of charge-density waves. *Rev. Mod. Phys.* **60**, 1129–1181 (1988).
- Carpinelli, J. M., Weitering, H. H., Plummer, E. W. & Stumpf, R. Direct observation of a surface charge density wave. *Nature* **381**, 398–400 (1996).
- Yildirim, T. Ferroelectric soft phonons, charge density wave instability, and strong electron-phonon coupling in BiS_2 layered superconductors: a first-principles study. *Phys. Rev. B* **87**, 020506 (2013).
- Zhang, Y., Yang, H. X., Ma, C., Tian, H. F. & Li, J. Q. Charge-stripe order in the electronic ferroelectric LuFe_2O_4 . *Phys. Rev. Lett.* **98**, 247602 (2007).
- Castro Neto, A. H. Charge density wave, superconductivity, and anomalous metallic behavior in 2D transition metal dichalcogenides. *Phys. Rev. Lett.* **86**, 4382–4385 (2001).
- Yu, F. H. et al. Unusual competition of superconductivity and charge-density-wave state in a compressed topological kagome metal. *Nat. Commun.* **12**, 3645 (2021).
- Wandel, S. et al. Enhanced charge density wave coherence in a light-quenched, high-temperature superconductor. *Science* **376**, 860–864 (2022).
- Nie, L. et al. Charge-density-wave-driven electronic nematicity in a kagome superconductor. *Nature* **604**, 59–64 (2022).
- Aishwarya, A. et al. Magnetic-field-sensitive charge density waves in the superconductor UTe_2 . *Nature* **618**, 928–933 (2023).
- Gooth, J. et al. Axionic charge-density wave in the Weyl semimetal $(\text{TaSe}_4)_2\text{I}$. *Nature* **575**, 315–319 (2019).
- Teng, X. et al. Magnetism and charge density wave order in kagome FeGe . *Nat. Phys.* **19**, 814–822 (2023).
- Teng, X. et al. Discovery of charge density wave in a kagome lattice antiferromagnet. *Nature* **609**, 490–495 (2022).
- Liu, L. et al. Direct identification of Mott Hubbard band pattern beyond charge density wave superlattice in monolayer 1T-NbSe_2 . *Nat. Commun.* **12**, 1978 (2021).
- Calandra, M. Phonon-assisted magnetic mott-insulating state in the charge density wave phase of single-layer 1T-NbSe_2 . *Phys. Rev. Lett.* **121**, 026401 (2018).
- Nakata, Y. et al. Robust charge-density wave strengthened by electron correlations in monolayer 1T-TaSe_2 and 1T-NbSe_2 . *Nat. Commun.* **12**, 5873 (2021).
- Zhu, X., Cao, Y., Zhang, J., Plummer, E. W. & Guo, J. Classification of charge density waves based on their nature. *Proc. Natl. Acad. Sci. USA* **112**, 2367–2371 (2015).
- Snijders, P. C. & Weitering, H. H. Colloquium: electronic instabilities in self-assembled atom wires. *Rev. Mod. Phys.* **82**, 307–329 (2010).
- Ahn, J. R., Yeom, H. W., Yoon, H. S. & Lyo, I. W. Metal-insulator transition in Au atomic chains on Si with two proximal bands. *Phys. Rev. Lett.* **91**, 196403 (2003).
- Ahn, J. R. et al. Mechanism of gap opening in a triple-band peierls system: In atomic wires on Si. *Phys. Rev. Lett.* **93**, 106401 (2004).
- Kumpf, C. et al. Low-temperature structure of indium quantum chains on silicon. *Phys. Rev. Lett.* **85**, 4916–4919 (2000).
- Frigge, T. et al. Optically excited structural transition in atomic wires on surfaces at the quantum limit. *Nature* **544**, 207–211 (2017).
- Yeom, H. W. et al. Instability and charge density wave of metallic quantum chains on a silicon surface. *Phys. Rev. Lett.* **82**, 4898–4901 (1999).
- Pandey, J. & Soni, A. Electron-phonon interactions and two-phonon modes associated with charge density wave in single crystalline 1T-VSe_2 . *Phys. Rev. Res.* **2**, 033118 (2020).
- Zheng, F. & Feng, J. Electron-phonon coupling and the coexistence of superconductivity and charge-density wave in monolayer NbSe_2 . *Phys. Rev. B* **99**, 161119 (2019).
- Xi, X. et al. Strongly enhanced charge-density-wave order in monolayer NbSe_2 . *Nat. Nanotechnol.* **10**, 765–769 (2015).
- Zhu, X., Guo, J., Zhang, J. & Plummer, E. Misconceptions associated with the origin of charge density waves. *Adv. Phys. X* **2**, 622–640 (2017).
- Ma, L. et al. A metallic mosaic phase and the origin of Mott-insulating state in 1T-TaS_2 . *Nat. Commun.* **7**, 10956 (2016).
- Yu, F. H. et al. Concurrence of anomalous Hall effect and charge density wave in a superconducting topological kagome metal. *Phys. Rev. B* **104**, L041103 (2021).
- Luo, H. et al. Electronic nature of charge density wave and electron-phonon coupling in kagome superconductor KV_3Sb_5 . *Nat. Commun.* **13**, 273 (2022).
- Li, H. et al. Observation of unconventional charge density wave without acoustic phonon anomaly in kagome superconductors AV_3Sb_5 ($\text{A} = \text{Rb}, \text{Cs}$). *Phys. Rev. X* **11**, 031050 (2021).

32. Zhang, F. et al. Atomic-scale manipulation of polar domain boundaries in monolayer ferroelectric In_2Se_3 . *Nat. Commun.* **15**, 718 (2024).
33. Zhou, Y. et al. Out-of-plane piezoelectricity and ferroelectricity in layered $\alpha\text{-In}_2\text{Se}_3$ nanoflakes. *Nano Lett.* **17**, 5508–5513 (2017).
34. Ding, W. et al. Prediction of intrinsic two-dimensional ferroelectrics in In_2Se_3 and other $\text{III}_2\text{-VI}_3$ van der Waals materials. *Nat. Commun.* **8**, 14956 (2017).
35. Huang, Y.-T. et al. Mexican-hat potential energy surface in two-dimensional $\text{III}_2\text{-VI}_3$ materials and the importance of entropy barrier in ultrafast reversible ferroelectric phase change. *Appl. Phys. Rev.* **8**, 031413 (2021).
36. Ortiz, B. R. et al. CsV_3Sb_5 : a Z_2 topological kagome metal with a superconducting ground state. *Phys. Rev. Lett.* **125**, 247002 (2020).
37. Zhao, R. et al. Tuning phase transitions in 1T-TaS_2 via the substrate. *Nano Lett.* **17**, 3471–3477 (2017).
38. Johannes, M. D. & Mazin, I. I. Fermi surface nesting and the origin of charge density waves in metals. *Phys. Rev. B* **77**, 165135 (2008).
39. Si, J. G. et al. Origin of the multiple charge density wave order in 1T-VSe_2 . *Phys. Rev. B* **101**, 235405 (2020).
40. Weber, F. et al. Extended phonon collapse and the origin of the charge-density-wave in 2H-NbSe_2 . *Phys. Rev. Lett.* **107**, 107403 (2011).
41. Zheng, C. et al. Room temperature in-plane ferroelectricity in van der Waals In_2Se_3 . *Sci. Adv.* **4**, eaar7720 (2018).
42. Xu, C. et al. Two-dimensional antiferroelectricity in nanostripe-ordered In_2Se_3 . *Phys. Rev. Lett.* **125**, 047601 (2020).
43. Wu, Z., Liu, K., Mu, X. & Zhou, J. Renormalizing antiferroelectric nanostripes in $\beta'\text{-In}_2\text{Se}_3$ via optomechanics. *J. Phys. Chem. Lett.* **14**, 677–684 (2023).
44. Zhang, F. et al. Atomic-scale observation of reversible thermally driven phase transformation in $2\text{D In}_2\text{Se}_3$. *ACS Nano* **13**, 8004–8011 (2019).
45. Chen, N.-K. et al. Directional forces by momentumless excitation and order-to-order transition in peierls-distorted solids: the case of GeTe . *Phys. Rev. Lett.* **120**, 185701 (2018).
46. Müller, P. C., Ertural, C., Hempelmann, J. & Dronskowski, R. Crystal orbital bond index: covalent bond orders in solids. *J. Phys. Chem. C* **125**, 7959–7970 (2021).
47. Tan, H., Liu, Y., Wang, Z. & Yan, B. Charge density waves and electronic properties of superconducting kagome metals. *Phys. Rev. Lett.* **127**, 046401 (2021).
48. Calandra, M., Mazin, I. I. & Mauri, F. Effect of dimensionality on the charge-density wave in few-layer 2H-NbSe_2 . *Phys. Rev. B* **80**, 241108 (2009).
49. Chen, P. et al. Unique gap structure and symmetry of the charge density wave in single-layer VSe_2 . *Phys. Rev. Lett.* **121**, 196402 (2018).
50. Miller, D. C., Mahanti, S. D. & Duxbury, P. M. Charge density wave states in tantalum dichalcogenides. *Phys. Rev. B* **97**, 045133 (2018).
51. Yang, Y. et al. Enhanced superconductivity upon weakening of charge density wave transport in 2H-TaS_2 in the two-dimensional limit. *Phys. Rev. B* **98**, 035203 (2018).
52. Ryu, H. et al. Persistent charge-density-wave order in single-layer TaSe_2 . *Nano Lett.* **18**, 689–694 (2018).
53. Jiang, T. et al. Two-dimensional charge density waves in TaX_2 ($\text{X} = \text{S}, \text{Se}, \text{Te}$) from first principles. *Phys. Rev. B* **104**, 075147 (2021).
54. Liu, M. et al. Multimorphism and gap opening of charge-density-wave phases in monolayer VTe_2 . *Nano Res.* **13**, 1733–1738 (2020).
55. Tresca, C. & Calandra, M. Charge density wave and spin $1/2$ insulating state in single layer 1T-NbS_2 . *2D Mater.* **6**, 035041 (2019).
56. Lin, H. et al. Scanning tunneling spectroscopic study of monolayer 1T-TaS_2 and 1T-TaSe_2 . *Nano Res.* **13**, 133–137 (2020).
57. Kolekar, S., Bonilla, M., Ma, Y., Diaz, H. C. & Batzill, M. Layer- and substrate-dependent charge density wave criticality in 1T-TiSe_2 . *2D Mater.* **5**, 015006 (2018).
58. Chen, G. et al. Correlating structural, electronic, and magnetic properties of epitaxial VSe_2 thin films. *Phys. Rev. B* **102**, 115149 (2020).
59. Zhang, D. et al. Strain engineering a $4a \times \sqrt{3}a$ charge-density-wave phase in transition-metal dichalcogenide 1T-VSe_2 . *Phys. Rev. Mater.* **1**, 024005 (2017).
60. Kresse, G. & Furthmüller, J. Efficient iterative schemes for ab initio total-energy calculations using a plane-wave basis set. *Phys. Rev. B* **54**, 11169–11186 (1996).
61. Kresse, G. & Joubert, D. From ultrasoft pseudopotentials to the projector augmented-wave method. *Phys. Rev. B* **59**, 1758–1775 (1999).
62. Kresse, G. & Furthmüller, J. Efficiency of ab-initio total energy calculations for metals and semiconductors using a plane-wave basis set. *Comput. Mater. Sci.* **6**, 15–50 (1996).
63. Heyd, J., Scuseria, G. E. & Ernzerhof, M. Hybrid functionals based on a screened Coulomb potential. *J. Chem. Phys.* **118**, 8207–8215 (2003).
64. Nosé, S. A unified formulation of the constant temperature molecular dynamics methods. *J. Chem. Phys.* **81**, 511–519 (1984).
65. Nelson, R. et al. LOBSTER: local orbital projections, atomic charges, and chemical-bonding analysis from projector-augmented-wave-based density-functional theory. *J. Comput. Chem.* **41**, 1931–1940 (2020).
66. Wang, V., Xu, N., Liu, J.-C., Tang, G. & Geng, W.-T. VASPKIT: a user-friendly interface facilitating high-throughput computing and analysis using VASP code. *Comput. Phys. Commun.* **267**, 108033 (2021).
67. Togo, A. & Tanaka, I. First principles phonon calculations in materials science. *Scr. Mater.* **108**, 1–5 (2015).

Acknowledgements

This work was supported by the National Science and Technology Major Project of China (Grant No. 2022ZD0117600, X.-B.L.), the National Natural Science Foundation of China (Grants No. 12274172, X.-B.L. and 12274180, N.-K.C.), the China Postdoctoral Science Foundation (Grant No. BX20240136, Y.-T.H. and GZB20240341, Z.-Z.L.), and the Natural Science Foundation of Jilin Province (20230101007JC, N.-K.C.). High-Performance Computing Center (HPCC) at Jilin University is also acknowledged. The authors thank Chen Si for helpful discussions. Z.-Z. L. is grateful for the support by the Shuimu Tsinghua Scholar Program.

Author contributions

Y.-T.H. and Z.-Z.L. predicted the CDW of $2\text{D In}_2\text{Se}_3$. Y.-T.H., X.-B.L., N.-K.C., and Z.-Z.L. conceived the calculations, Y.-T.H. performed the calculations. Y.-T.H., Z.-Z.L., X.-B.L., N.-K.C., and S.Z. did the theoretical analysis. Y.-T.H., Z.-Z.L., and X.-B.L. wrote the initial draft. H.-B.S. and Y.W. discussed the results and reviewed the manuscript. X.-B.L. and N.-K.C. supervised the project.

Competing interests

The authors declare no competing interests.

Additional information

Supplementary information The online version contains supplementary material available at <https://doi.org/10.1038/s41467-024-54205-1>.

Correspondence and requests for materials should be addressed to Nian-Ke Chen or Xian-Bin Li.

Peer review information *Nature Communications* thanks Chenggang Tao, and the other, anonymous, reviewer(s) for their contribution to the peer review of this work. A peer review file is available.

Reprints and permissions information is available at <http://www.nature.com/reprints>

Publisher's note Springer Nature remains neutral with regard to jurisdictional claims in published maps and institutional affiliations.

Open Access This article is licensed under a Creative Commons Attribution 4.0 International License, which permits use, sharing, adaptation, distribution and reproduction in any medium or format, as long as you give appropriate credit to the original author(s) and the source, provide a link to the Creative Commons licence, and indicate if changes were made. The images or other third party material in this article are included in the article's Creative Commons licence, unless indicated otherwise in a credit line to the material. If material is not included in the article's Creative Commons licence and your intended use is not permitted by statutory regulation or exceeds the permitted use, you will need to obtain permission directly from the copyright holder. To view a copy of this licence, visit <http://creativecommons.org/licenses/by/4.0/>.

© The Author(s) 2024